Acta Cryst. (1992). A48, 674-688

Dynamical Simulations of Energy-Filtered Inelastic Electron Diffraction Patterns

BY Z. L. WANG*

Metals and Ceramics Division, Oak Ridge National Laboratory, PO Box 2008, Oak Ridge, TN 37831-6376, USA, and Department of Materials Science and Engineering, The University of Tennessee, Knoxville, TN 37996-2200, USA

(*Received 6 November* 1991; *accepted 4 March* 1992)

Abstract

The previously proposed inelastic scattering theory [Wang (1991). *Acta Cryst.* A47, 686-698] has been applied to simulate the diffraction patterns of phonon, plasmon-loss and atomic core-shell scattered electrons. The details of the calculation method and the program flow chart are described here. The calculated thermal diffuse scattering (TDS) patterns using full lattice dynamics agree well with the experimental observations for parallel- and convergent-beam-illumination cases. The results have shown that the Kikuchi pattern is mainly produced by phonon-scattered electrons and that the Einstein model is not a good thermal-vibration model, at least for molybdenum and silicon. Under strongly diffracting conditions, calculations for energy-filtered diffraction patterns of core ionization edges have shown that the elastic and inelastic scattering can no longer be considered as independent and that the angular distribution of the inelastically scattered electrons cannot be simply described by the Lorentzian function. All these dynamical effects can affect the compositional microanalysis in electron energy-loss spectroscopy (EELS).

1. Introduction

Studies of inelastic electron diffraction are of great importance for developing new microscopy techniques and understanding the basic physics of electron scattering. Theoretically, a proper measurement of electron scattering from a crystal lattice with 'time-dependent' inelastic perturbation requires huge calculations using the available theories, such as the Bloch wave and multislice theories (Howie, 1963; Wang, 1990), because the excitation of each inelastic state of particular energy and momentum needs to be treated separately and incoherently. From the semiclassical viewpoint, thermal diffuse scattering, for example, is the result of statistically averaged quasi-elastic electron scattering from crystal lattices of different instantaneous 'frozen' configurations. Many important results have been obtained based on the Einstein model, in which the atomic vibrations are assumed to be random and there are no definite phase correlations, and on other simplified models (Bird & Wright, 1989; Cowley, 1988; Doyle, 1970; Fanidis, Van Dyck, Coene & Van Landuyt, 1989; Gjønnes, 1966; Gjønnes & Watanabe, 1966; Hall & Hirsch, 1965; Høier, 1973; Loane, Xu & Silcox, 1991; Rez, Humphreys & Whelan, 1977; Rossouw, 1985; Rossouw & Bursill, 1985; Whelan, 1965*a*, *b*). It is still necessary, for a generalized phonon excitation model with definite phase-correlation patterns, to find a method that can 'analytically' average over the scattering intensities from all these different lattice configurations before performing the numerical calculations to save computation time. Such a method has been derived (Wang, 1991, 1992; Wang & Bentley, 1991*a*, *b*).

In this paper, the previously proposed theory (Wang, 1991, 1992) is applied to simulate the energy-filtered diffraction patterns of phonon, single-electron and plasmon-loss scattered electrons under the single inelastic scattering approximation. The basic theory and the calculation method are introduced in §§ 2 and 3. The calculated results for molybdenum and silicon are compared with experimental observations (§ 4) and the validity of Einstein model is examined. Finally, the simulations for energy-filtered electron diffraction patterns of core ionization edges and the associated dynamical effects on compositional microanalysis in electron energy-loss spectroscopy (EELS) are outlined in § 5.

2. Basic inelastic electron scattering theory

Inelastic electron scattering is usually classified as four different processes. Plasmon (or valence) excitation, which characterizes the transition of electrons from the valence band to the conduction band, involves an energy loss in the range of 5-30 eV and an angular spread of less than 0.2 mrad for high-energy electrons. Atomic core-shell excitations introduce an energy loss in the range of a few hundreds to thousands of eV with an angular spread of the order $\theta_E = \Delta E/2E_0$, where ΔE is the electron energy loss and E_0 is the incident electron energy. Thermal diffuse scattering (TDS) or phonon scattering does not intro-

* Address for correspondence: Metals and Ceramics Division, Oak Ridge National Laboratory, Bldg 5500, MS 6376, PO Box 2008, Oak Ridge, TN 37831-6376, USA.

0108-7673/92/050674-15$06.00

duce any significant energy loss but produces large momentum transfer, which can scatter the electrons into the large-angle range. The last, but least-discussed, process is the *Bremsstrahlung* radiation, which is a continuous energy-loss process and is partly responsible for the background intensity at high-energy-loss regions in EELS. As a basis for the discussion in this paper, the major steps taken in the development of the new dynamical theory are briefly reviewed here. A detailed derivation can be found in Wang (1991, 1992).

The basic equation governing inelastic electron scattering in a crystal was derived from wave mechanics (Yoshioka, 1957). If Ψ_0 describes the elastically scattered wave of energy E and Ψ_n describes the inelastically scattered wave of energy E_n, with $n = 1, 2, \ldots$, under the single inelastic approximation, the generation and scattering of the inelastic wave is governed by

$$[\nabla^2 + k_n^2 + (2m_0 e/\hbar^2) V(\mathbf{r})]\Psi_n \simeq (2m_0/\hbar^2) H'_{n0}(\mathbf{r})\Psi_0, \quad (1)$$

where k_n is the electron wave vector, V is the crystal potential and H' is the inelastic scattering interaction Hamiltonian. With the assumption that electron scattering angles are of the same magnitude as Bragg angles, analogous to Howie's (1963) method, the solution of (1) can be written in the form

$$\Psi_n \equiv \varphi_n(\mathbf{r})\Psi_n^0(\mathbf{r}), \quad (2)$$

where $\Psi_n^0(\mathbf{r})$ is the solution for an elastic wave of free-space wave vector $\mathbf{k}_n$, which satisfies the boundary conditions $\Psi_n^0(x, y, 0) = \exp(i\mathbf{k}_n \cdot \mathbf{r})$ and the elastic-scattering Schrödinger equation

$$[\nabla^2 + k_n^2 + (2m_0 e/\hbar^2) V(\mathbf{r})]\Psi_n^0 = 0, \quad (3)$$

and $\varphi_n(\mathbf{r})$ is a three-dimensional function characterizing the inelastic-scattering effects. Equation (3) can be solved using either the Bloch-wave method or the multislice method. Substituting (2) into (1), using (3), neglecting the $\partial^2\varphi_n(\mathbf{r})/\partial z^2$ term under the small-angle approximation and ignoring the $\partial\varphi_n(\mathbf{r})/\partial x$ and $\partial\varphi_n(\mathbf{r})/\partial y$ terms, since $k_{x,y} \ll k_z$, where $\mathbf{k} = (k_x, k_y, k_z)$ is the wave vector, one obtains

$$\partial\varphi_n(\mathbf{r})/\partial z \simeq \alpha H'_{n0}(\mathbf{r})\Psi_0^0(\mathbf{r})[\partial\Psi_n^0(\mathbf{r})/\partial z]^{-1}\varphi_0(\mathbf{r}), \quad (4)$$

where $\alpha = m_0/\hbar^2$. For thin crystals such that $\varphi_0(\mathbf{r}) \simeq 1$, the first-order solution of (4) is

$$\varphi_n(\mathbf{b}, z) = \alpha\left[\int_0^z dz_1 H'_{n0}(\mathbf{b}, z_1, \mathbf{q}) S_n(\mathbf{b}, z_1)\right]. \quad (5a)$$

Combining this result with (2), one obtains

$$\Psi_n(\mathbf{b}, z) = \alpha\left[\int_0^z dz_1 H'_{n0}(\mathbf{b}, z_1, \mathbf{q}) S_n(\mathbf{b}, z_1, \mathbf{q})\right]\Psi_n^0(\mathbf{b}, z), \quad (5b)$$

where

$$S_n(\mathbf{r}, \mathbf{q}) = \Psi_0^0(\mathbf{r})/[\partial\Psi_n^0(\mathbf{r})/\partial z]. \quad (5c)$$

It has been shown (Wang, 1991) that (5*b*) is equivalent to the inelastic-scattering multislice theory. Equation (5*b*) has been applied to phonon excitations based on the semiclassical 'frozen lattice' model (Wang & Bentley, 1991*a*) and the full lattice dynamics (Wang, 1992) case. The theoretical results have successfully interpreted the positions and intensities of TDS streaks observed in electron diffraction patterns. Further applications of (5*b*) have provided a simple theory that accounts for valence-excitation effects in simulating high-resolution electron-microscopy images (Wang & Bentley, 1991*b*,*c*).

Phase correlations among the inelastic events (or states) critically affect the intensity distribution in the diffraction pattern but do not affect the image contrast formed by the inelastically scattered electrons under the first-order approximation (Cowley, 1988; Wang, 1992), so that the Einstein model can be used for image simulations. This is the reason that the simulations of inelastic electron diffraction patterns are more complex than image simulations. Now one considers the energy-filtered diffraction pattern of inelastically scattered electrons after exciting a particular state. Taking a two-dimensional Fourier transform of (5*b*), with $\boldsymbol{\tau} = (\tau_x, \tau_y)$ in reciprocal space, and characterizing the perturbation of $\mathbf{q}$ to the elastic wave Ψ_n^0 by an average momentum transfer $\mathbf{q}_0$ (the validity of this approximation is discussed in § 3.5), one obtains

$$\Psi_n(\boldsymbol{\tau}, d) \simeq \alpha\int_0^d dz\, H'_{n0}(\boldsymbol{\tau}, z, \mathbf{q}) \otimes S_n(\boldsymbol{\tau}, z', \mathbf{q}_0) \otimes \Psi_n^0(\boldsymbol{\tau}, d, \mathbf{q}_0), \quad (6)$$

where $\otimes$ represents the convolution operation. For a three-dimensional periodic crystal structure of reciprocal-lattice vector $\mathbf{g}$, H' can be written as (Howie, 1963)

$$H'_{n0}(\mathbf{r}, \mathbf{q}) = \exp(i\mathbf{q} \cdot \mathbf{r}) \sum_g H'_g(\mathbf{g} - \mathbf{q}) \exp(-i\mathbf{g} \cdot \mathbf{r}) \quad (7a)$$

or

$$H'_{n0}(\boldsymbol{\tau}, z, \mathbf{q}) = [(2\pi)^2/A] \exp(iq_z z) \sum_g H'_g(\mathbf{g} - \mathbf{q})\delta(\boldsymbol{\tau} - \mathbf{g} + \mathbf{q}_b), \quad (7b)$$

where H'_g is the Fourier coefficient of H', and A is the cross section of the unit cell perpendicular to the z axis. Substituting (7*b*) into (6), summing the incoherent intensities contributed by the inelastic-scattering processes of different $\mathbf{q}$'s but the same energy loss and neglecting the coupling between different

g's, one obtains

$$I(\tau)=[V_c/(2\pi)^3]\int_{BZ} d\mathbf{q}|\Psi_n(\tau,d)|^2$$
$$\simeq[V_c/(2\pi)^3](4\pi^2\alpha/A)^2\sum_g\int_{BZ} d\mathbf{q}|H'_g(\mathbf{g}-\mathbf{q})|^2$$
$$\times|Z(\tau-\mathbf{g}+\mathbf{q}_b,q_z,\mathbf{q}_0)|^2, \quad (8a)$$

where the integration of $\mathbf{q}$ is restricted to the first Brillouin zone (BZ); $\mathbf{q}_0$ is introduced to represent the average momentum transfer in inelastic electron scattering; the subscript b refers to the projection of the corresponding quantity in the xy plane;

$$Z(\tau,\mathbf{q}_0)\equiv\left[\int_0^d dz\exp(iq_zz)S_n(\tau,z,\mathbf{q}_0)\right]$$
$$\otimes\Psi_n^0(\tau,d,\mathbf{q}_0). \quad (8b)$$

Equation (8a) can be further simplified by separating the integration of $\mathbf{q}$ into $\mathbf{q}_b=(q_x,q_y)$ and q_z. By the definition of a function

$$T(\tau)\equiv[a_3\theta(\tau)/2\pi]\sum_g\int_{BZ} dq_z|H'_g(\tau,q_z)|^2, \quad (9a)$$

where a_3 is the lattice constant in the z direction and

$$\theta(\tau)\equiv\begin{cases}1 \text{ if } \tau \text{ falls within the first Brillouin zone (BZ)}\\ 0 \text{ otherwise,}\end{cases} \quad (9b)$$

the integration of $\mathbf{q}_b$ in (8a) can thus be extended to $(-\infty,\infty)$ in reciprocal space. Since q_z is mainly related to the electron energy loss by $q_z\simeq k_0(E-E_1)/2E$, independent of $\mathbf{q}_b$ (Egerton, 1986), to a good approximation one can take Z out of the integration of q_z and thus

$$I(\tau)\simeq\xi^2\int_{-\infty}^{\infty} d\mathbf{q}_bT(\mathbf{g}-\mathbf{q}_b)|Z(\tau-\mathbf{g}+\mathbf{q}_b,\mathbf{q}_0)|^2$$
$$=\xi^2T(\tau)\otimes|Z(\tau,\mathbf{q}_0)|^2, \quad (10)$$

where $\xi=2\pi\alpha/A^{1/2}$. The effect of $\mathbf{q}$ in S_n and Ψ_n^0 is represented by the effect of a mean value $\mathbf{q}_0$. This is the key step for simplification of the inelastic calculation. The validity of this approximation is discussed in § 3.5. The S_n function is the key part of the dynamical calculations, which is responsible for the formation of Kikuchi patterns (see § 3.1). Equation (10) can be applied to different inelastic-scattering processes, such as phonon, single-electron and valence excitations. The corresponding T functions for these processes have been given in an earlier paper (Wang, 1991). Here we concentrate on the numerical calculations using (10) for TDS.

3. Diffraction patterns of phonon-scattered electrons

Phonon scattering is generated by atomic vibrations in the crystal. Thermal vibrations introduce a time-dependent displacement to each atom, resulting in a small perturbation of the crystal potential. With the atomic displacement expressed in the normal coordinate system under the harmonic oscillators approximation, the corresponding T function for TDS is derived (Wang, 1991) as

$$T^{(TDS)}=a_3e^2(2\pi)^5\theta(\tau)$$
$$\times\sum_j\sum_l\int_{BZ} dq_z[\hbar/2\omega_j(\tau)m_l]$$
$$\times|[\mathbf{e}(l|_j^\tau)\cdot\tau]V_l(\tau)|^2, \quad (11)$$

where j and l are the summations over all the phonon branches of dispersion surface $\omega_j(\tau)$ and the atoms of mass m_l and scattering factor $V_l(\tau)$ (including the Debye–Waller factor) within the atomic unit cell, respectively, and $\mathbf{e}(l|_j^\tau)$ is the phonon polarization vector. It is important to note that the variation of the phonon dispersion relation $\omega_j(\tau)$, particularly for acoustic modes, can produce sharp intensity variations across the diffraction pattern, resulting in the formation of TDS streaks as observed experimentally. The details of applying (10) and (11) to the dynamical calculations of TDS electrons are described in the next section.

3.1. *Calculations of Z function in the multislice scheme*

As shown by (10), the primary dynamical scattering effects are contained in the Z function. The first step in the calculation of the Z function is to find the full dynamical solution of Ψ_0^0. In this study, the multislice theory is employed to solve the elastic-scattering equation (3). For the inelastically scattered waves, the localized inelastic scattering generated from different crystal slices (or depths) is treated as being incoherent, so that

$$|Z(\tau,\mathbf{q}_0)|^2\simeq\Delta z^2\sum_i|S_n(\tau,z_i,\mathbf{q}_0)\otimes\Psi_0^0(\tau,d,\mathbf{q}_0)|^2, \quad (12)$$

where $\Psi_0^0(\tau,d,\mathbf{q}_0)$ is the elastic transmission wave of free-space wave vector $\mathbf{k}-\mathbf{q}_0$ at the crystal exit face and the summation is over crystal slices i of equal thickness Δz. Since Ψ_n^0 is responsible for the intensity distribution of the elastic Bragg reflections, which will not be significantly affected by the inelastic excitation, Ψ_n^0 has been replaced by Ψ_0^0 in (12). To reduce the computation time, one neglects the perturbation effect of $\mathbf{q}_0$ on the elastic wave Ψ_0^0, so that (12) can be approximately written as

$$|Z(\tau,\mathbf{q}_0)|^2\simeq\Delta z^2\sum_i|S_n(\tau,z_i,\mathbf{q}_0)\otimes\Psi_0^0(\tau,d)|^2. \quad (13)$$

In the multislice approach, a crystal is cut into many slices in the z direction and the atomic structure in each slice is projected onto a plane perpendicular to the z axis. It is not straightforward to find $\partial\Psi_0^0(\mathbf{r},\mathbf{q})/\partial z$ directly from Ψ_0^0 in the multislice approach. For this reason, one starts from the original elastic-scattering equation (3). By writing

$\Psi_0^0(\mathbf{b}, z, \mathbf{q}) \equiv \varphi_0^0(\mathbf{b}, z, \mathbf{q}) \exp[i(\mathbf{k}-\mathbf{q})\cdot\mathbf{r}]$, where $\mathbf{k}=(k_x, k_y, k_z)$ is the electron wave vector, and neglecting the $\partial^2\varphi_0^0/\partial z^2$ term, (3) becomes

$$\frac{\partial\varphi_0^0}{\partial z} = -\left\{\frac{2m_0e}{\hbar^2}V\varphi_0^0 + \left[\frac{\partial^2}{\partial x^2}+\frac{\partial^2}{\partial y^2}\right]\varphi_0^0 + 2i\left[k_x\frac{\partial}{\partial x}+k_y\frac{\partial}{\partial y}\right]\varphi_0^0\right\}\Big/ 2ik_z, \quad (14)$$

so that

$$\begin{aligned} S_n(\mathbf{r},\mathbf{q}) &\equiv \Psi_0^0(\mathbf{r})/[\partial\Psi_0^0(\mathbf{r},\mathbf{q})/\partial z] \\ &= \varphi_0^0(\mathbf{r})\exp(-i\mathbf{q}\cdot\mathbf{r})/[ik_z\varphi_0^0(\mathbf{r},\mathbf{q})+\partial\varphi_0^0(\mathbf{r},\mathbf{q})/\partial z] \\ &= \varphi_0^0(\mathbf{r})\exp(-i\mathbf{q}\cdot\mathbf{r}) \\ &\quad\times\left\{ik_z\varphi_0^0(\mathbf{r},\mathbf{q}) - \frac{1}{2ik_z}\left[\frac{2m_0e}{\hbar^2}V(\mathbf{r})\varphi_0^0(\mathbf{r},\mathbf{q}) + \left(\frac{\partial^2}{\partial x^2}+\frac{\partial^2}{\partial y^2}\right)\varphi_0^0(\mathbf{r},\mathbf{q}) + 2i\left(k_x\frac{\partial}{\partial x}+k_y\frac{\partial}{\partial y}\right)\varphi_0^0(\mathbf{r},\mathbf{q})\right]\right\}^{-1}. \end{aligned} \quad (15)$$

For high-energy electrons, the first term in the curly brackets of (15) is much larger than the remaining terms, thus

$$S_n(\mathbf{r},\mathbf{q}) \simeq \varphi_0^0(\mathbf{r})\exp(-i\mathbf{q}\cdot\mathbf{r})/ik_z\varphi_0^0(\mathbf{r},\mathbf{q}). \quad (16)$$

As will be shown by numerical calculations (§ 3.4), the S_n function is responsible for the formation of Kikuchi lines. The multislice solution of φ_0^0 (Cowley & Moodie, 1957; Ishizuka & Uyeda, 1977; Ishizuka, 1982) is

$$\varphi_0^0(\mathbf{b}, z+\Delta z, \mathbf{q}) = [\varphi_0^0(\mathbf{b}, z, \mathbf{q})Q_q(\mathbf{b}, z)] \otimes P_q(\mathbf{b}, \mathbf{q}), \quad (17a)$$

where Q_q is the phase grating function of the crystal slice Δz,

$$Q_q(\mathbf{b}, z) = \exp\left[i(\sigma k_z/k)\int_z^{z+\Delta z} dz' V(\mathbf{b}, z')\right]; \quad (17b)$$

the wave propagation function is

$$P_q(\mathbf{b}, \mathbf{q}) = (k_z/i\Delta z\lambda k)\exp(i\pi|\mathbf{b}-\mathbf{b}_0|^2/2\lambda\Delta z); \quad (17c)$$

$\sigma = e/\hbar v_0$; v_0 is the electron velocity; λ is the electron wavelength of energy E; $k_z=(k^2-q^2)^{1/2}$; $\mathbf{b}_0=(\Delta z/k_z)\mathbf{q}$ introduced by the inclined incident effect of the beam. The multislice solution of $\varphi_0^0(\mathbf{b}, z)$ similarly follows (17a-c) for $\mathbf{q}=0$. Finally, the Z function can be obtained by substituting the calculated S_n function and $\varphi_0^0(\mathbf{b}, z)$ for different crystal slices into (13). This is the core part of the computation program.

3.2. *Total absorption coefficient of TDS*

In TDS calculations, the relative contribution of TDS to the final diffraction pattern is normalized according to the total absorption coefficient of the elastic-scattering wave, since the total scattered intensity must be conservative. The absorption effect introduced by the phonon-scattering process is now considered. If the elastic-scattering wave can be written analogously to (2) as

$$\Psi_0 = \varphi_0(\mathbf{r})\Psi_0^0(\mathbf{r}), \quad (18a)$$

where Ψ_0^0 is the full solution of (3) without considering any absorption, the absorption introduced by inelastic scattering is contained in $\varphi_0(\mathbf{r})$, which is determined (Wang, 1991) by

$$\partial\varphi_0(\mathbf{r})/\partial z = \alpha\sum_{m\neq 0} H'_{0m}(\mathbf{r})S_m(\mathbf{r})\varphi_m(\mathbf{r}), \quad (18b)$$

where the sum over m is over all the excited states. Since the elastic scattering of the electrons after inelastic scattering (*i.e.* the process for forming a Kikuchi pattern) will not affect the calculation of the total absorption coefficient, one can take S_m [defined in (5c) and (16)] as a constant, which means there is no elastic scattering after inelastic excitation. Substituting (5a) into (18b), one gets

$$\partial\varphi_0(\mathbf{b}, z)/\partial z \simeq -(\alpha^2/k_z^2)\sum_{m\neq 0} H'_{0m}(\mathbf{b}, z)\int_0^z dz' H'_{m0}(\mathbf{b}, z'). \quad (19)$$

For TDS, H'_{0m} is either a real or an imaginary function, so that $H'_{m0}=H'^{*}_{0m}$ holds. Integrating (19) and using the boundary condition $\varphi_0(\mathbf{b}, z=0)=1$, one obtains

$$\begin{aligned} \varphi_0(\mathbf{b}, z) &= 1-(\alpha^2/2k_z^2)\sum_{m\neq 0}\left|\int_0^z dz' H'_{m0}(\mathbf{b}, z')\right|^2 \\ &\simeq \exp\left\{-(\alpha^2/2k_z^2)\sum_{m\neq 0}\left|\int_0^z dz' H'_{m0}(\mathbf{b}, z')\right|^2\right\}, \end{aligned} \quad (20)$$

where the crystal is assumed thin so that the absorption factor is small. Substituting the interaction Hamiltonian for TDS in (20), changing the summation of m to $[V_c/(2\pi)^3]\sum_{j=1}^{3n_0}\int_{BZ} d\mathbf{q}$, where n_0 is the number of atoms in the primitive unit cell, and using the Einstein model, one finally has (Wang & Bentley, 1991c)

$$\varphi_0(\mathbf{b}, z) = \exp\left\{-\frac{e^2\alpha^2}{2k^2}\sum_l \overline{A_1^2}\left[\left(\frac{\partial v_l[\mathbf{b}-\mathbf{r}_b(l)]}{\partial x}\right)^2 + \left(\frac{\partial v_l[\mathbf{b}-\mathbf{r}_b(l)]}{\partial y}\right)^2\right]\right\}, \quad (21)$$

where the summation of l is limited to the atoms located in the thickness range from $z=0$ to $z=z$; v_l is the projected atomic potential of the lth atom;

$\overline{A_l^2}$ is the mean square atomic-vibration amplitude. Finally, the total TDS absorption coefficient for a crystal of thickness d is the integration of the exponential term in (21),

$$C_{abs}=\frac{e^2\alpha^2}{2k_z^2 s}\sum_l \overline{A_l^2}\int \mathrm{d}\mathbf{b}\left[\left(\frac{\partial v_l(\mathbf{b})}{\partial x}\right)^2+\left(\frac{\partial v_l(\mathbf{b})}{\partial y}\right)^2\right], \quad (22)$$

where s is the area of the crystal slice plane. This is the equation to be used for normalizing the total TDS intensity.

3.3. *Calculation method and program flow chart*

A dynamic program has been written based on Ishizuka's (1982) multislice program for simulating high-resolution electron-microscopy images. The most important advantage of the original program is that the calculation for an inclined incident beam can be conveniently performed without changing the way of cutting crystal slices, providing an easy way for calculating the elastic wave of wave vector $\mathbf{k}-\mathbf{q}$. A flow chart of the program is shown in Fig. 1, in which the original multislice program is taken as a 'subroutine' for calculating the elastic wave. The major steps in the program are described as follows.

The phase grating and propagation functions for the normal incident (Q_0 and P_0) and the inclined incident (Q_q and P_q) electrons following (17*b*) and (17*c*), respectively, are calculated in step 1. The TDS generation function T is calculated in step 2 from (11). The atomic scattering factor $V_l(\tau)$ is converted from an X-ray scattering factor following the Mott formula and considering the Debye-Waller factor. For monoatomic crystals under the central-force approximation, the phonon dispersion relationships given by Born (1942) for cubic systems are used. The calculation of the total absorption coefficient in step 3 follows (22), which will be used for normalizing the final TDS intensity. In step 4, the final elastic wave for the normal-incidence case [$\varphi_F^0=\varphi_0^0(\mathbf{b}, d)$] at the crystal exit face is calculated following the normal multislice operations. This function needs to be calculated first because it will be used in the TDS wave calculation for each slice [see (13)]. The incident electron wave is assumed to be a parallel beam, *i.e.* in the reciprocal space the beam is a δ function (for the computational process it is just one pixel point). The elastic electron diffraction pattern is calculated and output at step 5.

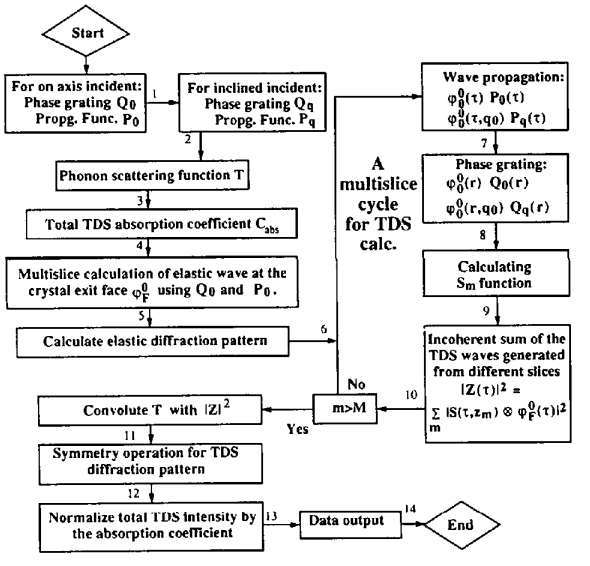

Fig. 1. A flow chart of the TDS dynamical calculation program.

Step 6 is a multislice cycle for calculating the $|Z|^2$ function, consisting of steps 7 to 10. Steps 7 and 8 are designed to calculate the $\varphi_0^0(\mathbf{r})$ and $\varphi_0^0(\mathbf{r}, \mathbf{q}_0)$ wave functions following (17). The S function is calculated according to (15). The inverse-Fourier-transform technique is used to perform the calculation of the Laplace operator. Then the convolution of the S_n function with $\Psi_0^0(\boldsymbol{\tau}, d)$ (in reciprocal space) and the incoherent summation of the convoluted result for each slice are performed in step 10. The calculations involved in steps 7 to 10 are repeated for each crystal slice until the desired maximum crystal-slice number (M) is reached. Then in step 11, according to (10), the $|Z|^2$ function is convoluted with the phonon-scattering function calculated in step 2. Since the mean momentum transfer $\mathbf{q}_0$ introduced in the initial calculation is a vector, the calculated result is rotated, in step 12, according to the symmetry of the crystal zone axis to perform the symmetric angular average of the momentum transfer. In step 13, the total TDS intensity is normalized with respect to the elastically scattered intensity according to the absorption coefficient calculated in step 3. Finally the TDS diffraction pattern is output in step 14.

In the simulations for Mo [001] TDS diffraction patterns, a large unit cell was chosen with dimensions 31.4×31.4 Å (the lattice constant for Mo is 3.14 Å), which was separated into 256×256 pixels. The slice thickness was 1.57 Å. The incident electron beam was assumed to be a plane wave. To compensate for the effects of ignoring momentum transfer in the elastic wave Ψ_0^0 from (12) to (13), a small background, less than 0.5% of the height of the central (000) beam and limited to the first BZ, was introduced in the initial incident elastic wave. All the calculations assumed 100 keV electrons. The mean vibration amplitudes for Mo and Si were taken as 0.08 and 0.09 Å respectively. The calculation takes approximately 13 h for a 600 slice diffraction pattern on a DEC station 5000/200. The calculated pattern is displayed on a logarithmic scale to enhance the visibility of weak features at high angles.

In the following analysis, the experimental diffraction patterns were taken with a Philips EM400/FEG (100 keV) transmission electron microscope and

recorded on photographic plates. Since the response of the film plate to the electron intensities of different dose rates is actually an unknown nonlinear function, it is difficult to make a digital quantitative comparison between the calculated and the observed patterns, but some good agreements can still be obtained.

3.4. *Calculated TDS diffraction pattern*

For a perfect crystal, pure elastic interaction only scatters the electrons at the angles satisfying the Bragg reflection condition and there is no intensity between the Bragg spots (Fig. 2*a*). However, electrons can be scattered by phonons at different angles, forming a visible Kikuchi pattern in reciprocal space. TDS streaks are produced and distributed even to larger angles where Bragg reflections are relatively weak (Fig. 2*b*). It is clear that inelastic scattering is responsible for the detailed intensity distribution in the diffraction pattern. The sum of the elastic and TDS patterns gives the final pattern, which can be compared with the energy-filtered zero-loss pattern recorded using the microscope.

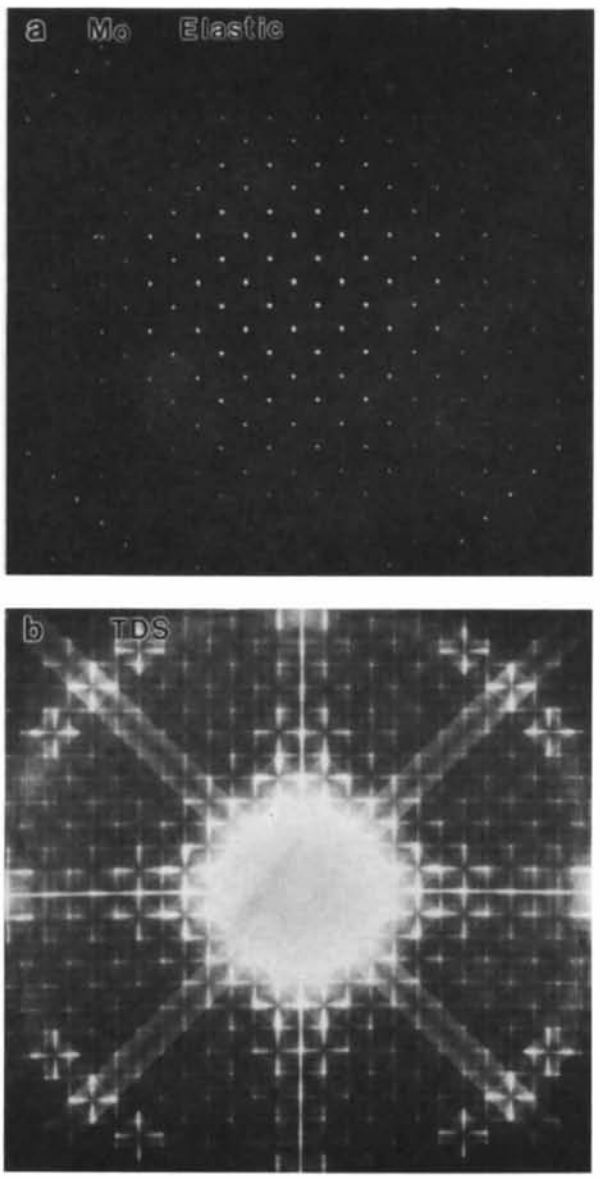

Fig. 2. Simulated (*a*) elastically and (*b*) phonon-scattered electron diffraction patterns of Mo [001] for the nonconvergent incident-beam case. The crystal thickness is 1884 Å, the beam energy is 100 keV and the mean momentum transfer $q_0 = 8.32 \times 10^{-3}\, k$, where k is the electron wave vector.

A comparison of a simulated electron diffraction pattern of molybdenum [001] with an experimentally observed pattern is shown in Fig. 3. The experimental pattern shown in Fig. 3(*b*) is an unfiltered diffraction pattern containing the contributions from the electrons that had experienced various elastic and inelastic scattering processes, such as plasmon excitation. The TDS streaks would appear sharper if an energy filter was used (Reimer, Fromm & Naundorf, 1990). The simulated pattern is a sum of the contributions from purely elastically scattered electrons and phonon-scattered electrons. The Bragg spots near 000 are much stronger than the TDS streaks. The observed Kikuchi pattern is not as sharp as the calculated one because the specimen foil was bent. The pattern was taken from a large thin foil under the parallel-illumination condition, since a selected-area aperture could not be used for taking these patterns because its use limits the contribution of large-angle scattered electrons. The TDS streaks clearly appear along ⟨010⟩ and ⟨100⟩ directions and are the results of phase coupling between atomic vibrations. In other words, these TDS streaks should not show up if the Einstein model is valid. The weak diffuse ring along the first-order Laue zone (FOLZ) is also seen but the Bragg spots along the FOLZ ring are not in the correct positions, being shifted by {100}. This is because the phase shift of each slice in the z direction was not considered in the multislice calculation, resulting in incorrect forbidden reflection conditions for the FOLZ. This effect can be properly considered in the calculation but needs a large amount of disk memory and computation power (Self & O'Keefe, 1989). In addition, a larger crystal thickness is used in the calculation to match the observed Kikuchi pattern of a relatively thin crystal. This is because the multiple plasmon and *Bremsstrahlung* scattering, not being considered in the calculation, are contained in the experimental patterns and would produce a strong uniform Kikuchi-line background.

For silicon, it is relatively easy to obtain a large area of thin unbent perfect crystal. A comparison of a simulated elastic and TDS silicon [001] electron diffraction pattern with an observed one is shown in Fig. 4. The TDS streaks along ⟨110⟩ are clearly shown, which indicate that the Einstein model of random phase vibration is not a good approximation for Si.

In graphics displays of electron diffraction patterns, the large difference in intensity magnitude makes the selection of the appropriate gray level difficult. A display of the calculated pattern in Fig. 4(*a*) that is limited to low-index reflections only is shown in Fig. 5. The {220} and {400} Kikuchi bands and the TDS streaks are clearly shown.

For the convergent-beam case, however, the situation may be different. The increase of the beam convergence is equivalent to convoluting the TDS streaks with the beam angular spread (Fig. 6*a*), resulting in a uniform and featureless intensity background in the diffraction pattern, as shown in Fig. 6(*b*). The Kikuchi pattern is clearly produced by TDS. When the elastic and TDS patterns are added, the final pattern agrees well with the experimental observed one except for some differences at the FOLZ as discussed above (Fig. 7). It is coincidental that the observed convergent-beam pattern appears to be about the same as that expected from the Einstein

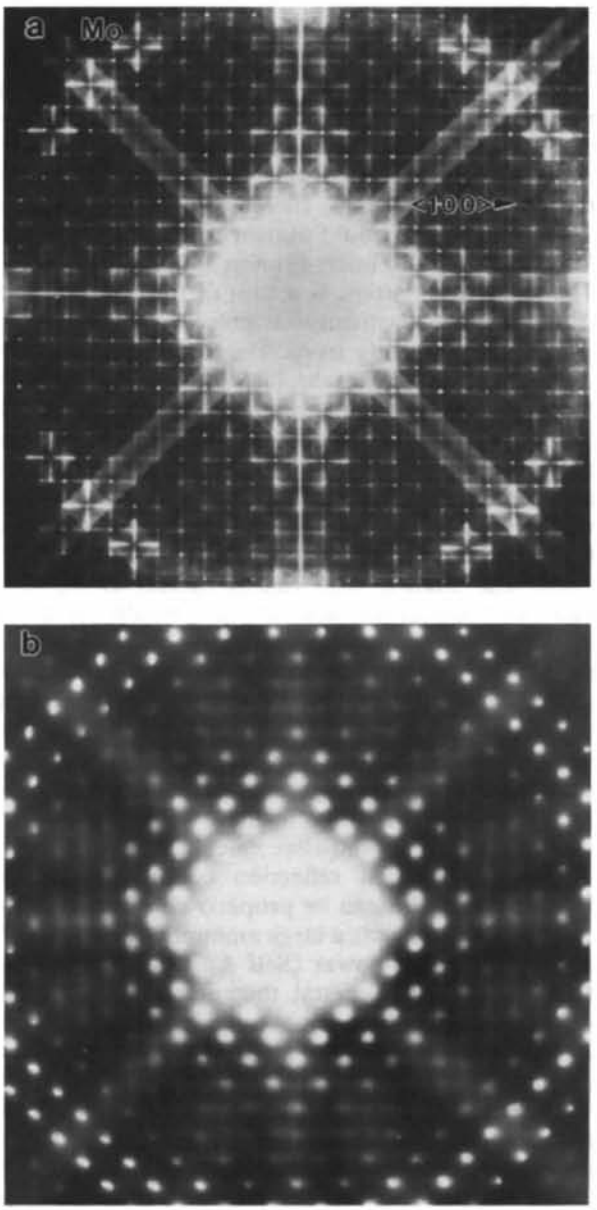

Fig. 3. Comparison of (*a*) a simulated and (*b*) an observed Mo [001] electron diffraction pattern under the parallel-beam illumination condition. The crystal thickness is 1884 Å and the mean momentum transfer $q_0 = 8.32 \times 10^{-3}$ *k*. The simulated diffraction pattern is the total contributions from elastic and phonon scattering. The TDS streaks along ⟨010⟩ and ⟨100⟩ can be seen.

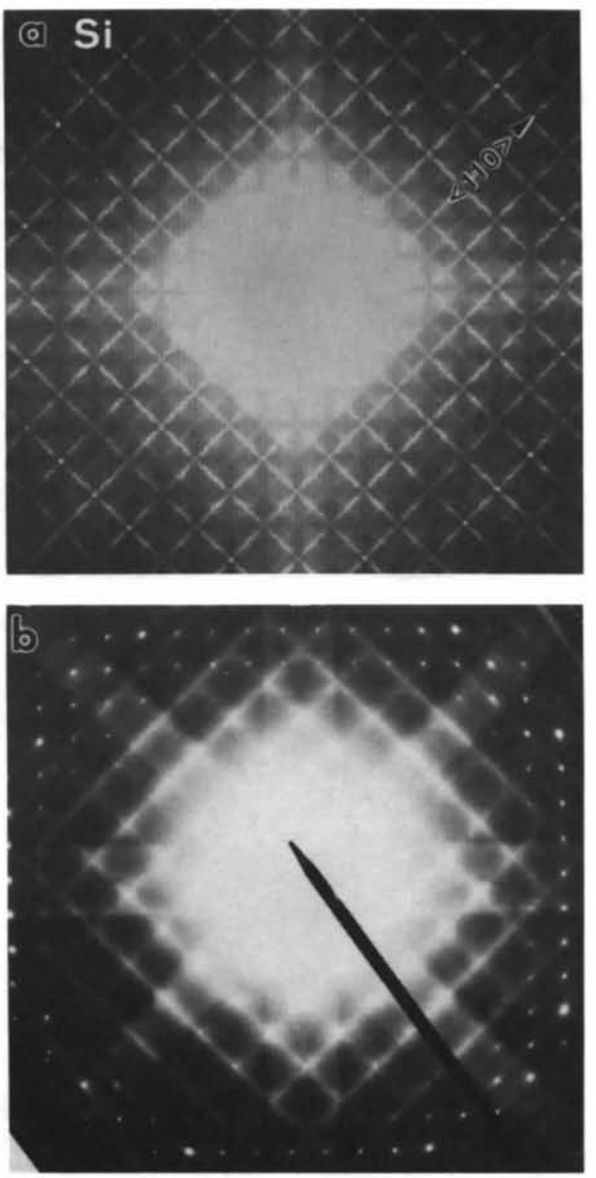

Fig. 4. Comparison of (*a*) a simulated and (*b*) an observed Si [001] electron diffraction pattern for the parallel incident-beam case. The crystal thickness is 2443 Å and the mean momentum transfer $q_0 = 9.62 \times 10^{-3}$ *k*. The TDS streaks along ⟨110⟩ can be seen.

model because the fine TDS streaks have been smeared out by the beam convergence; this does not mean that the Einstein model is valid for silicon.

3.5. *Selection of the mean momentum transfer* $\mathbf{q}_0$

In inelastic scattering, the conical angular distribution of the electrons after inelastic scattering is the source of the formation of Kikuchi lines in the diffraction patterns, the inelastic electrons just satisfying the Bragg law producing the dark–white line pairs due to dynamical scattering. The size of the angular cone is determined by the momentum transfer of the electrons during inelastic scattering. In the above calculations, the perturbation effect of momentum transfer in the elastic-wave calculation was characterized by the effect of a mean value $\mathbf{q}_0$. The question is then: how does the selection of $\mathbf{q}_0$ affect the calculated TDS pattern? The following calculations may provide some answers.

If $\mathbf{q}_0$ is chosen to be zero, which means that the inelastic scattering does not introduce any angular redistribution, Kikuchi patterns should not be seen but TDS streaks should be observed. This is exactly the calculated result shown in Fig. 8, in which the TDS streaks at large scattering angles are not as strong as those calculated for relatively large q_0 as shown in Fig. 3(a). By increasing the value of q_0 to $4.14\times 10^{-3}\,k$, the Kikuchi pattern is formed but the TDS streaks are visible only at relatively low scattering angles and the FOLZ shows up strongly (Fig. 9a). If q_0 is further increased to the maximum value within the first BZ, the TDS-streak intensity is enhanced at large angles but the FOLZ intensity is washed out (Fig. 9b). It seems that the selection of $\mathbf{q}_0$ has to be optimized by observing the relative intensities of the TDS streaks with respect to that of the FOLZ in reference to the experimental observations. A reasonable choice of q_0 would be between $4.14\times 10^{-3}\,k$ and $1.66\times 10^{-2}\,k$. This was the principle that was followed in the calculations for Mo and Si in Figs. 3–6. Furthermore, it has been found that the Kikuchi pattern is not dramatically affected by the crystal thickness if it is larger than approximately 70 nm. This may be because steady-state Bloch waves are established when the crystal is thicker than this value. It seems that the introduction of $\mathbf{q}_0$ significantly simplifies the inelastic calculations, and reasonable results can still

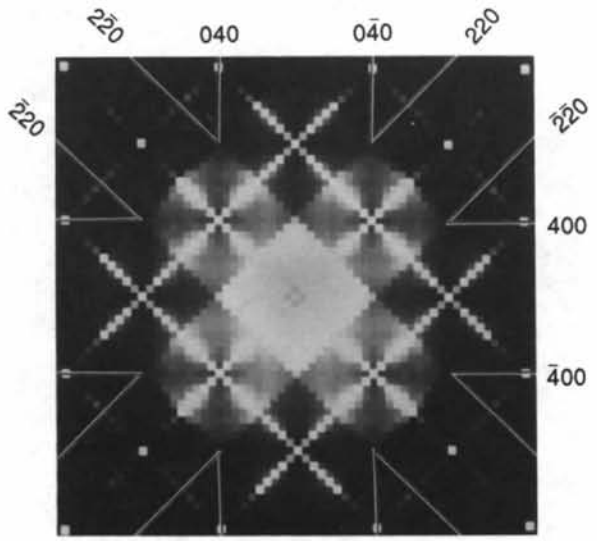

Fig. 5. The calculated pattern of Fig. 4(a) for low-angle reflections only.

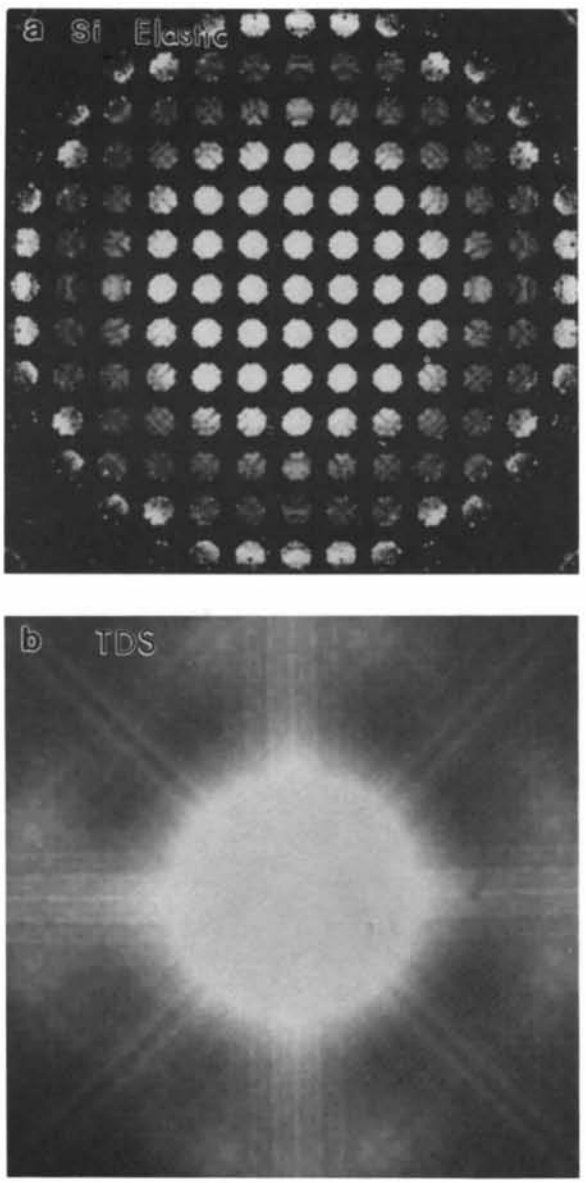

Fig. 6. Simulated (a) elastically and (b) phonon-scattered electron diffraction patterns of Si [001] for the convergent-beam case of conical half-angle 4.5 mrad. The crystal thickness is 2443 Å and the mean momentum transfer $q_0 = 9.62\times 10^{-3}\,k$.

be obtained. This confirms the validity of the approximation of replacing $\mathbf{q}$ by $\mathbf{q}_0$ in the calculations of S_n and Ψ_0^0 [see (6)].

4. Energy-filtered diffraction patterns of valence-loss electrons

Valence (or plasmon) losses are generated by collective excitations of the electrons in the crystal. This process usually involves small energy losses (about 10–30 eV) and small momentum transfers. Since (7*a*) is valid only for localized inelastic scattering, it is necessary to reconsider the diffraction of valence-loss electrons. It is shown in the Appendix that, for a homogeneous medium, (10) can still be applied to calculate the diffraction patterns of valence-loss electrons and the corresponding T function is given by

$$T^{(V)} \simeq [e^2\hbar V_s/\pi\varepsilon_0]\theta(\tau) \int_0^\infty d\omega \, \mathrm{Im}[-1/\varepsilon(\omega,\tau)] \times [\tau^2+(\omega/v_0)^2]^{-1}, \quad (23)$$

where V_s is the volume of the crystal. For common inorganic solids, the $\varepsilon(\omega,\tau)$ values are tabulated based on optical measurements (Palik, 1985). The program used for TDS calculation can be modified for valence-loss calculations simply by replacing $T^{(\mathrm{TDS})}$ with $T^{(V)}$ and q_0 with q_E ($q_E = \Delta Ek/2E_0$).

A calculated energy-filtered Si [001] diffraction pattern of the 15 eV volume plasmon loss is shown in Fig. 10(*a*). For comparison, Fig. 10(*b*) shows the calculated elastic diffraction pattern under the same conditions. Obviously, energy loss smears out the diffracting intensity. This agrees with the experimental observations of energy-filtered diffraction patterns of Reimer *et al.* (1990). The perturbation of the small angular spread of the plasmon loss on the S_n function seems to be significant.

5. Energy-filtered diffraction patterns of atomic inner-shell scattered electrons

The development of modern microscopy techniques has made it feasible to acquire energy-filtered electron diffraction patterns from core-shell excited electrons.

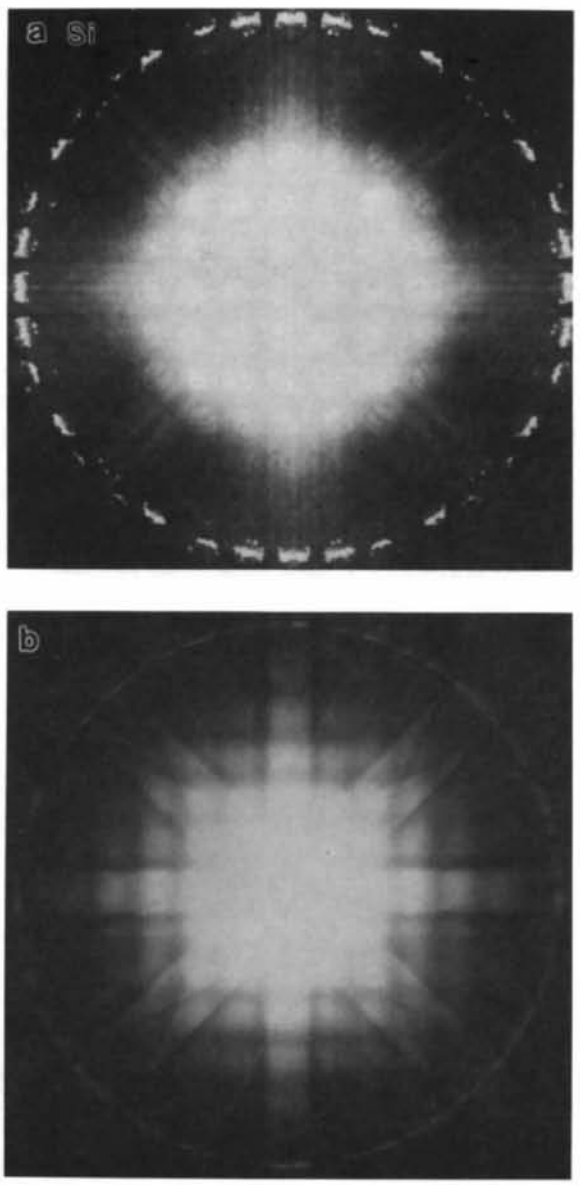

Fig. 7. Comparison of (*a*) a simulated and (*b*) an observed Si [001] electron diffraction pattern for convergent incident-beam case of conical half-angle 4.5 mrad. The crystal thickness is 2443 Å and the mean momentum transfer $q_0 = 9.62 \times 10^{-3}$ *k*.

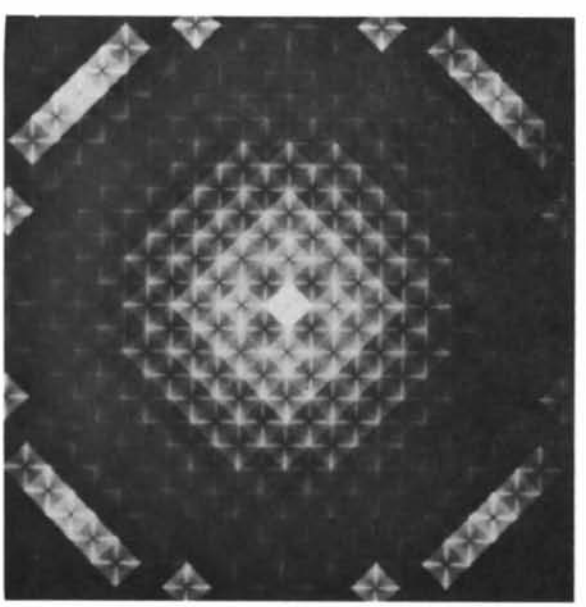

Fig. 8. A simulated Mo [001] TDS electron diffraction pattern for $q_0 = 0$. Other conditions are the same as for Fig. 3.

This type of inelastic electron diffraction pattern can also be simulated according to (10). Single-electron excitation is generated by exciting an atomic inner shell, resulting in a particular energy loss and momentum transfer. Since this process is mainly determined by the properties of each single atom, it is possible to use the tight-binding approximation, the final T function (Wang, 1991) being

$$T^{(S)} \simeq [e^2/V_c\varepsilon_0]^2(N\Re a_0^2/\Delta E) \times \left\{\sum_l |f'_{10}|\right\}[\theta(\tau)/(\tau^2+q_E^2)], \quad (24)$$

where $a_0 = 0.53$ Å is the Bohr radius, $\Re = 13.6$ eV is the Rydberg energy, f^l_{nm} is the generalized oscillator strength (GOS) of the lth atom, which is almost independent of the scattering angle, V_c is the volume of the crystal unit cell and $q_E = k\Delta E/(2E_0)$. For the energy-filtered diffraction patterns, the relative magnitude of the total single-electron excitation is not important, the only important quantity for $T^{(S)}$ is the angular-dependent part $\theta(\tau)/(\tau^2+q_E^2)$, thus the calculation of f^l_{nm} is avoided. The program used for TDS calculation can be modified for single-electron calculations simply by replacing $T^{(\mathrm{TDS})}$ with $T^{(S)}$ and q_0 with q_E.

For relatively low energy-loss core ionization edges, the excitation is mostly associated with the scattering of the outer-shell electrons through small scattering angles. A calculated Si L-edge ($\Delta E = 100$ eV) energy-filtered [001] diffraction pattern is shown in Fig. 11. It is clear that the pattern is remarkably diffused by the inelastic scattering and the Bragg

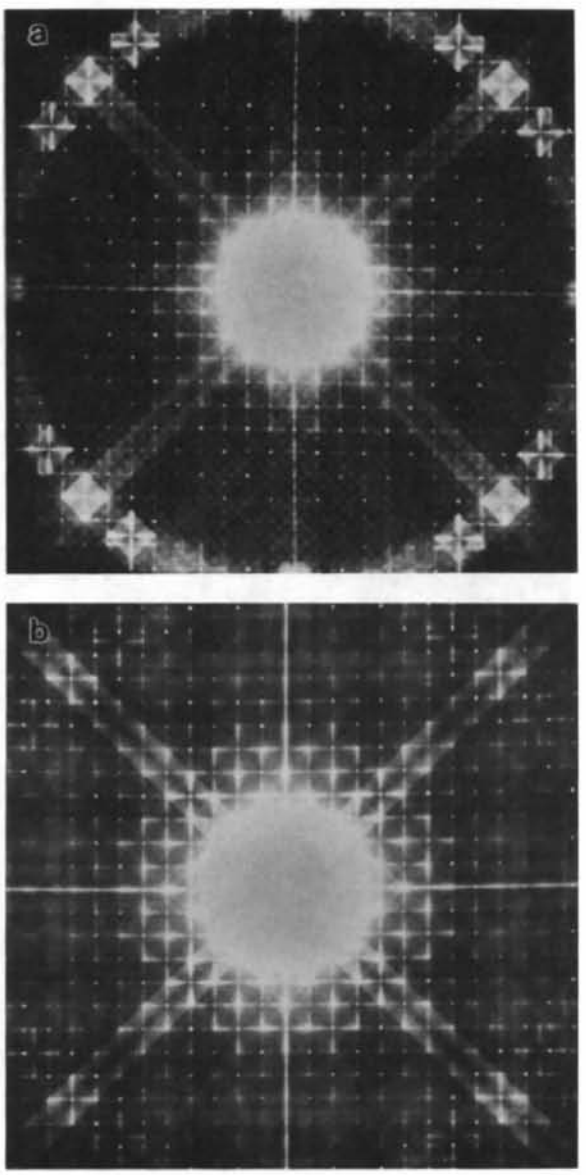

Fig. 9. Simulated Mo [001] diffraction patterns of elastically and phonon-scattered electrons for different mean momentum transfers: (*a*) $q_0 = 4.14\times10^{-3}\,k$ and (*b*) $q_0 = 1.66\times10^{-2}\,k$. Other conditions are the same as for Fig. 3.

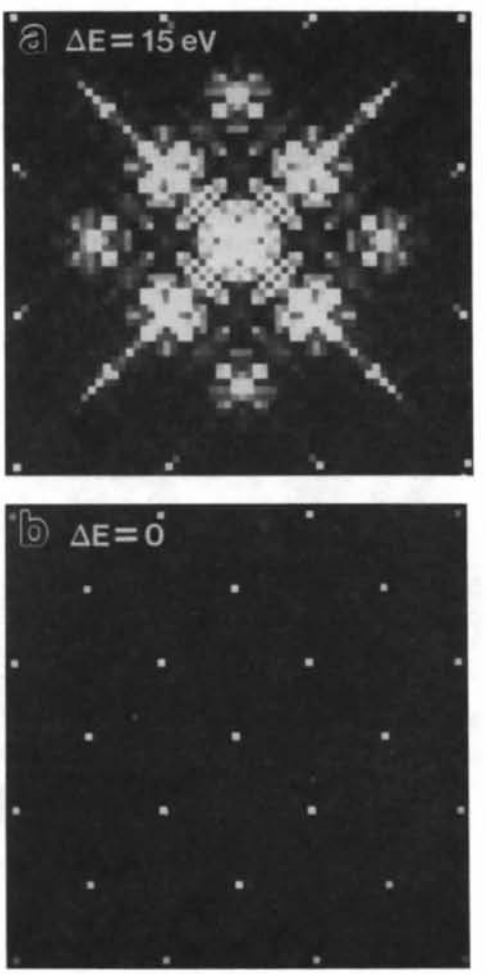

Fig. 10. Simulated Si [001] (*a*) energy-filtered plasmon-loss and (*b*) elastic electron diffraction patterns under the parallel-illumination condition. The crystal thickness is 543 Å.

spots are broadened by the angular distribution of the inelastic electrons. Since the incident beam was assumed to be a plane wave, the Kikuchi lines seen in the background are produced purely by the inelastic electrons. Sharp streaks, labeled with arrowheads, are seen passing through the (000) spot, midway between and parallel to the Kikuchi lines, which may be generated by the channeling electrons in the (100) and (110) atomic planes. In contrast to the diffuse low-index reflections, the intensity distribution at higher angles appears relatively sharp.

For high energy-loss ionization edges, the corresponding characteristic scattering angle could be larger than the smallest Bragg reflection angle, so that the entire pattern would be smeared out by the angular spreading of the inelastic scattering. A full dynamically calculated Si K-edge ($\Delta E = 1850$ eV) energy-filtered [001] pattern is shown in Fig. 12(a). The high-index Bragg reflections are broadened by the angular distribution of inelastic electrons. It appears that the channeling effect is even stronger for K-shell than for L-shell scattered electrons, resulting in the formation of sharp intensity streaks located midway between and parallel to the Kikuchi lines, as indicated by the arrowheads. This may be because the K-shell ionization edge can only be excited by electrons channeling close to the atomic nuclei. For greater contrast, the detailed intensity distribution at low scattering angles is shown in Fig. 13(a).

In EELS, it is always assumed that the elastic and inelastic scattering are independent, so that the intensity distribution in reciprocal space is a convolution of the inelastic angular-distribution function with the elastic Bragg-reflection intensity. This is the result of the dynamical elastic and kinematical inelastic scattering model. The corresponding calculation of this model can be performed simply by taking S_n as a δ function in reciprocal space [see (13)], and the calculated pattern under identical conditions as for Fig. 12(a) is shown in Fig. 12(b). The differences between Figs. 12(a) and (b) can be summarized as

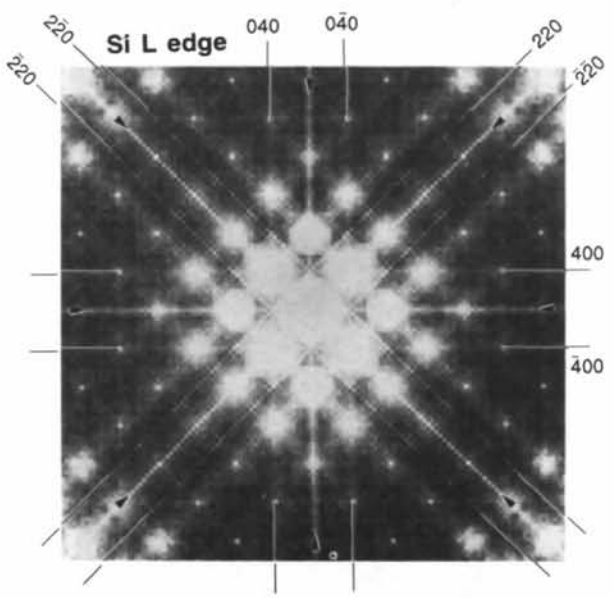

Fig. 11. A simulated Si [001] L-edge energy-filtered electron diffraction pattern. The beam convergence is zero, the crystal thickness is 1629 Å and $q_0 = q_E = 4.18 \times 10^{-4}\ k$. The sharp streaks appearing midway between the Kikuchi lines are indicated by arrowheads and may correspond to the channeling electrons in the (100) and (110) atomic planes.

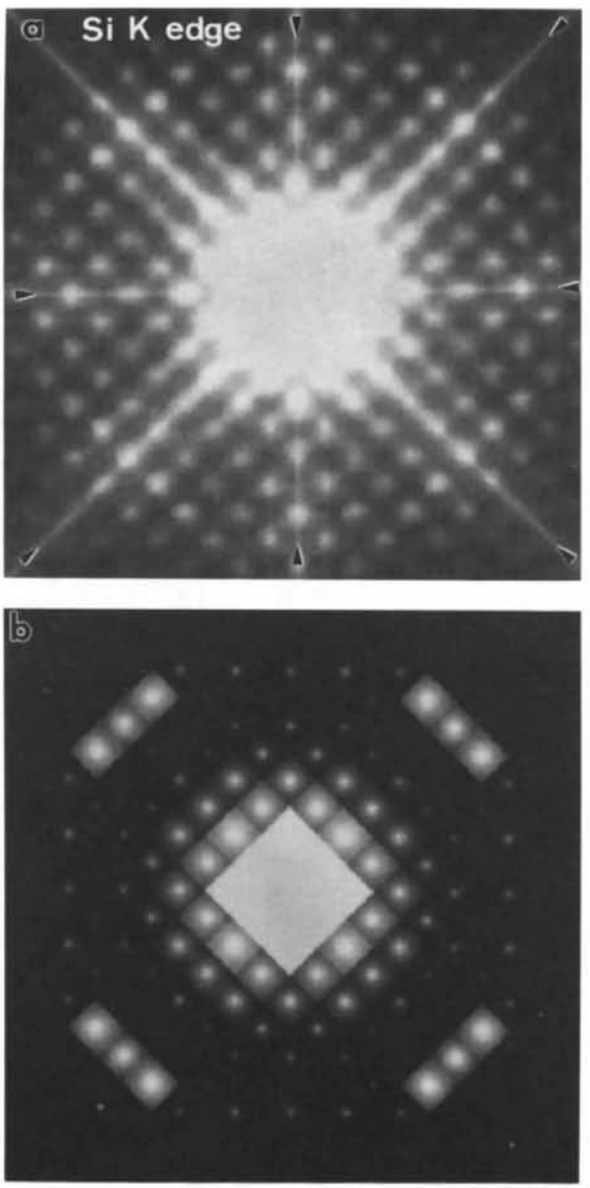

Fig. 12. The simulated Si [001] K-edge energy-filtered electron diffraction patterns using (a) the dynamical and (b) the kinematical inelastic scattering models. The beam convergence is zero, the crystal thickness is 1629 Å and $q_0 = q_E = 7.73 \times 10^{-3}\ k$. The sharp streaks appearing midway between the Kikuchi lines are indicated by arrowheads.

follows. Firstly, there is no sharp FOLZ in the full dynamically calculated pattern. For ease of understanding, the angular-spread effect of the inelastic scattering can be considered as being approximately equivalent to wobbling the origin of the Ewald sphere, so that all the Bragg reflections at high angles would be strongly and uniformly excited, which is equivalent to smearing out the intensity distribution of the FOLZ. Secondly, the kinematical inelastic scattering model does not produce Kikuchi patterns because the elastic rescattering of the electrons after inelastic scattering was neglected in this model. This proves that the S_n function is responsible for the formation of Kikuchi patterns. Finally, no strong intensity streaks are observed in the calculated pattern of the kinematical-scattering model. As pointed out above, the intensity streaks located midway between the Kikuchi lines are produced by the channeling electrons, which is a purely dynamical-scattering effect.

To show the fine details clearly, the intensity distributions at low reflection angles in Figs. 12(a) and (b) are redisplayed in Figs. 13(a) and (b), respectively. The corresponding contour plots of Figs. 13(a) and (b) are shown in Figs. 13(c) and (d), respectively. There are two major differences between Figs. 13(a) and (b). The first difference is the relative intensity of (200) to (000) - more intensity is concentrated on (000) in Fig. 13(b). This indicates that the dynamical scattering of the inelastic electrons can critically affect the intensity distribution in the entire diffraction pattern. Therefore, the elastic and inelastic scattering are no longer independent, especially for zone-axis cases. The other difference is that the angular distribution of the inelastically scattered electrons is not cylindrically symmetric [as seen in Fig. 13(c)] and cannot be described simply by the Lorentzian function, which is a cylindrically symmetrical function and is defined as $1/(\theta^2+\theta_E^2)$, where θ is the electron scattering angle. The accumulation of electrons along the (000)-{220} lines is the result of combined dynamical elastic and inelastic scattering. These factors can affect the compositional microanalysis in EELS for relatively large EELS entrance aperture, as described below.

In EELS, the chemical composition of a material can be derived if the elastic- and inelastic-scattering events are assumed to be independent. In zone-axis cases, however, apart from the channeling effect, this assumption is not correct based on the above

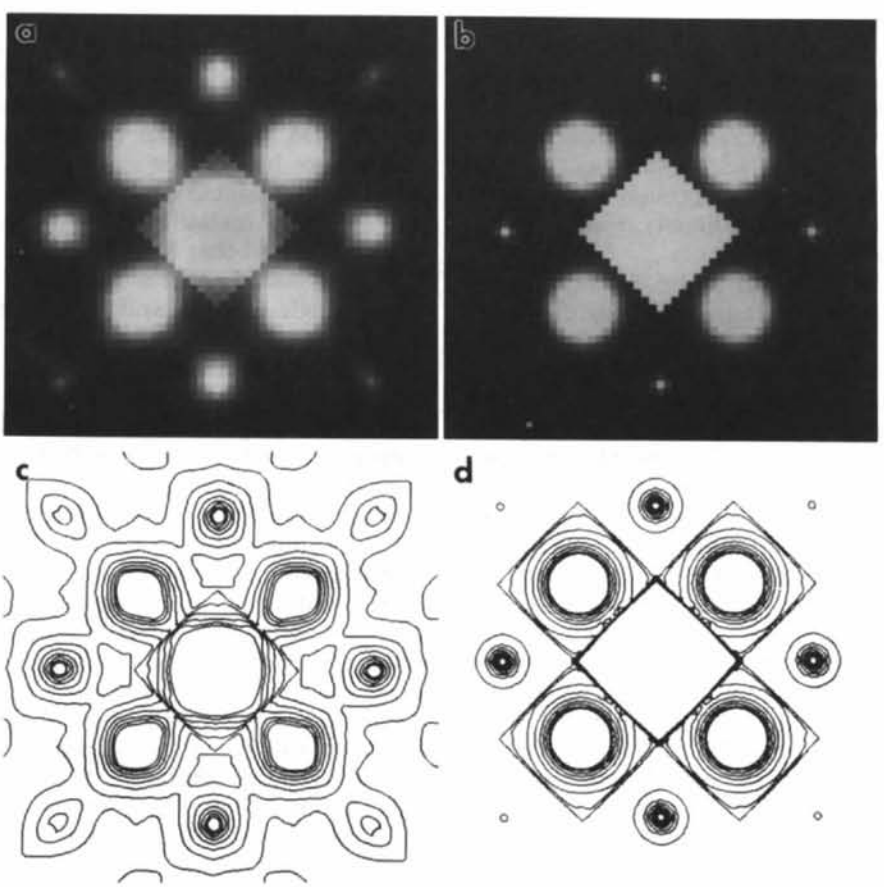

Fig. 13. (a), (b) The calculated patterns of Figs. 12(a) and (b), respectively, for low-index reflections only. (c), (d) The corresponding contour plots of (a) and (b), respectively.

calculation; the angular distribution of the inelastically scattered electrons cannot be described by the Lorentzian function, resulting in inaccuracies of the ionization cross-section calculations. In other words, the ionization cross section is not solely the property of a single atom, but depends on diffracting conditions and crystal structure. A possible method for correcting these effects is tilting the crystal to a 'random' orientation far away from the zone axis, along which no strong dynamical diffraction effects can be generated. Another possible way is to use a smaller EELS entrance aperture, which may eliminate the anisotropic distribution of the inelastic electrons.

However, in surface-composition microanalysis using the reflection electron energy-loss spectroscopy (REELS) technique, strongly diffracting conditions are mostly employed to improve the signal-to-background ratio and surface sensitivity (Wang & Bentley, 1991*d*). A possible solution in this case is to measure the effective ionization cross section by the method introduced by Wang & Bentley (1991*e*).

The calculated energy-filtered diffraction patterns described above can, in principle, be compared with the experimental observations. However, it is important to point out that the calculated patterns are the results of the core-shell purely inelastically scattered electrons without considering the contributions of the background electrons in EELS. In practice, it is possible to remove the contribution of background electrons by subtracting the energy-filtered patterns taken at the edge and before the edge and by considering the relative intensity of the background. The patterns processed in this way can be directly compared with the calculated ones.

The background electrons in EELS may be produced by the following inelastic-scattering processes. The first process is *Bremsstrahlung* radiation, which is a continuous energy-loss process. This process is generated by electrons penetrating through matter and undergoing collisions with the atoms. X-rays are often produced by a beam of electrons hitting a solid target. Most collision energy losses occur in small steps as fractional energy transfers, producing a continuous background in EELS spectra. The existence of this process can be seen in the background part of X-ray energy dispersion spectroscopy (EDS) spectra. The other process is the multiple valence excitations, which can produce large accumulated energy losses and momentum transfers, so that the final scattering angle may be larger than the Bragg angle, resulting in the formation of Kikuchi patterns as observed by Reimer *et al.* (1990). These two inelastic-scattering processes have not been considered in these calculations because of the limitation of computation power and the complexity of the processes. It is believed that the above two processes are responsible for the formation of a continuous background in EELS spectra, which needs to be removed to make quantitative analysis of energy-filtered diffraction patterns.

It is worth comparing the results calculated in this paper with those of Rossouw (1985). The Bloch-wave theory for inelastic scattering has been extensively developed by Rossouw and his co-workers for single-electron and TDS (using the Einstein model) excitations. However, the calculations addressed in this paper using a different theoretical approach may have the following advantages compared to their work. Firstly, the full lattice dynamics of atomic vibrations is employed in TDS calculations instead of the Einstein model. This allows the prediction of TDS streaks observed experimentally. Secondly, the parallel-beam-illumination case is assumed in the above calculations, so that the fine details introduced by phonon dispersion surfaces can be clearly resolved.

6. Concluding remarks

In this paper, the previously proposed inelastic-scattering theory has been used to simulate inelastic electron diffraction patterns after exciting various processes. In contrast to the 'frozen' lattice model, the calculations need to be performed only once for all the different crystal configurations. More importantly, it is feasible to introduce full lattice dynamics in the calculation, so that the experimentally observed TDS streaks could be simulated quantitatively. The observed TDS streaks can be used to determine the interactions between crystal atoms, leading to some information about crystal bonding properties. Based on the single inelastic-scattering approximation, it has been found that the TDS is the main source of forming Kikuchi patterns because of large scattering angle, single-electron and valence-band excitations contributing less intensity to the Kikuchi patterns. The multiple inelastic valence scattering and *Bremsstrahlung* radiation, which are believed to produce the background intensity at high-energy-loss regions in EELS, can contribute a strong diffuse Kikuchi-pattern background to the pattern.

With reference to the experimental observations, it has been found that the Einstein model is not a good approximation, at least for molybdenum and silicon. The deviation of the Einstein model from experimental results can be clearly seen in parallel-beam-illumination TDS patterns. In the convergent-beam case, the features introduced by acoustic phonon modes have been totally smeared out after convoluting with the beam convergence, the final results appearing quite similar to that expected from the Einstein model, but this does not mean that the Einstein model is valid in practice.

It has been shown that small energy losses, such as 15 eV, can significantly smear out the intensity distribution in the energy-filtered diffraction pattern. For zone-axis incident cases, the dynamical diffrac-

tion effects are so important that the elastic and inelastic scattering cannot be considered as independent; the kinematical inelastic scattering model is not valid and the angular distribution of the inelastically scattered electrons may not be simply described by the Lorentzian function. All these factors can affect the accuracy of EELS microanalysis under strongly diffracting conditions. In addition, calculations have also shown that sharp intensity streaks located midway between and parallel to the Kikuchi lines are produced by inelastic channeling electrons along the atomic planes.

The author is grateful to Dr J. Bentley for his support and encouragement. Thanks also go to Drs L. L. Horton, K. B. Alexander and L. F. Allard for comments. This research was sponsored by the Division of Materials Sciences, US Department of Energy, under contract DE-AC05-84OR21400 with Martin Marietta Energy Systems, Inc.

APPENDIX

Diffraction of valence-excited electrons

For delocalized valence excitation (7*a*) is no longer valid. It is necessary to consider the diffraction effect based on the mixed dynamic form factor. For valence excitations, one assumes that H'_{n0} is independent of z. At the crystal exit face $z = d$, (5*b*) can be rewritten as

$$\Psi_n(\mathbf{b}, d) = \alpha H'_{n0}(\mathbf{b}) Z(\mathbf{b}, \omega), \qquad (A.1)$$

where

$$Z(\mathbf{b}, \omega) = \int_0^d \mathrm{d}z \Psi_0^0(\mathbf{b}, z) / \{[\partial \Psi_0^0(\mathbf{b}, z, \omega)/\partial z] \Psi_0^0(\mathbf{b}, d, \omega)\}. \qquad (A.2)$$

To simplify the notation, $\Psi_n^0(\mathbf{b}, d)$ is replaced by $\Psi_0^0(\mathbf{b}, d, \omega)$, where $\hbar\omega$ is the electron energy loss. The change of symbol simply neglects the $\mathbf{q}$ dependence of Ψ_n^0 (*i.e.* presupposes that all states are nondegenerate). For small-angle plasmon excitation, the introduction of a small angular spread (less than 0.1 mrad) does not affect the final calculated results. Now one considers the energy-filtered diffraction patterns formed by the valence-excited electrons. One takes the Fourier transform of (*A*.2) and the contributions of all the valence-excited states to the final electron diffraction pattern are added *incoherently* in reciprocal space τ,

$$I_v(\tau) = \sum_n |\Psi_n(\tau, d)|^2 = (\alpha d/8\pi^3\varepsilon_0)^2 \sum_n |H'_{n0}(\tau) \otimes Z(\tau, \omega)|^2, \qquad (A.3)$$

where the sum of n is over all the possible valence states of different energies and different momenta. In general, for $n \neq 0$, the interaction of an external electron with a crystal can be stated as

$$H'_{n0}(\mathbf{r}) = \left\langle 0 \left| (1/4\pi\varepsilon_0) \times \left\{ \sum_j e^2/|\mathbf{r} - \mathbf{r}_j| - \sum_k Z_k e^2/|\mathbf{r} - \mathbf{R}_k| \right\} \right| n \right\rangle = (e^2/8\pi^3\varepsilon_0) \int \mathrm{d}\mathbf{u}/u^{-2} \exp(i\mathbf{u} \cdot \mathbf{r}) \rho_{n0}(\mathbf{u}), \qquad (A.4)$$

where $\mathbf{r}_j$ and $\mathbf{R}_k$ are the positions of the jth crystal electron and the kth nucleus respectively and

$$\rho_{n0}(\mathbf{u}) \equiv \langle 0 | \sum_j \exp(-i\mathbf{u} \cdot \mathbf{r}_j) | n \rangle. \qquad (A.5)$$

$\rho_{n0}(\mathbf{u})$ is the Fourier-transformed density operator in the Heisenberg representation and is usually a complex function associated directly with the electron distribution inside the crystal. By using (*A*.4) and expanding the convolution operation, one can rewrite (*A*.3) as

$$I_v(\tau) = C_0 \int \mathrm{d}\mathbf{u}_b \int \mathrm{d}\mathbf{u}'_b \times [Z(\tau - \mathbf{u}_b, \omega) Z^*(\tau - \mathbf{u}'_b, \omega)/u^2 u'^2] S(\mathbf{u}, \mathbf{u}'), \qquad (A.6)$$

where $C_0 = \alpha^2 e^4/\varepsilon_0^2$; $u^2 = u_b^2 + u_z^2$ with $u_z = q_n = k_0\hbar\omega/2\gamma E_0$ where γ is the relativistic correction factor, S is defined as the mixed dynamic form factor,

$$S(\mathbf{u}, \mathbf{u}') \equiv \sum_n \rho_{0n}(\mathbf{u}) \rho_{n0}(-\mathbf{u}'). \qquad (A.7)$$

For electron collective excitations, the mixed dynamic form factor is related to the generalized dielectric function by (Kohl & Rose, 1985)

$$S(\mathbf{u}, \mathbf{u}') = \int_{-\infty}^{\infty} \mathrm{d}\omega \{i\hbar\varepsilon_0 V_s/2\pi e^2 [1 - \exp(-\beta\hbar\omega)]\} \times [g^2/\varepsilon_{\mathbf{u}\mathbf{u}'}(\omega) - g'^2/\varepsilon^*_{\mathbf{u}'\mathbf{u}}(\omega)], \qquad (A.8)$$

where $\beta = 1/k_B T$, T is the temperature of the system and V_s is the volume of the crystal. Substituting (*A*.8) into (*A*.6), one obtains

$$I_v(\tau) = C_0 \int \mathrm{d}\mathbf{u}_b \int \mathrm{d}\mathbf{u}'_b Z(\tau - \mathbf{u}_b, \omega) Z^*(\tau - \mathbf{u}'_b, \omega) \times \int_{-\infty}^{\infty} \mathrm{d}\omega' \{i\hbar\varepsilon_0 V/2\pi e^2 [1 - \exp(-\beta\hbar\omega')]\} \times \{1/[u'^2 \varepsilon_{\mathbf{u}\mathbf{u}'}(\omega')] - 1/[u^2 \varepsilon^*_{\mathbf{u}'\mathbf{u}}(\omega')]\}. \qquad (A.9)$$

Assuming that the distribution of incident electrons inside the crystal is not significantly affected by a small energy loss, so that the Z function can be approximately included in the integration of ω' (in numerical calculations, this is actually an excellent approximation) and considering the condition $|\hbar\omega/k_B T| \gg 1$ for plasmon excitations, one finds that

(*A*.9) becomes

$$I_v(\tau) \simeq C_1 V \int \mathrm{d}\mathbf{u}_b \int \mathrm{d}\mathbf{u}'_b \int_0^\infty \mathrm{d}\omega (1/u'^2) \times \mathrm{Im}\{-[1/\varepsilon_{\mathbf{u}\mathbf{u}'}(\omega)] Z(\boldsymbol{\tau}-\mathbf{u}_b, \omega) \times Z^*(\boldsymbol{\tau}-\mathbf{u}'_b, \omega)\}, \quad (A.10)$$

where $C_1 = e^2 m_0^2/\pi\varepsilon_0\hbar^3$. Equation (*A*.10) is a generalized intensity distribution in the valence-loss electron diffraction pattern. Now consider a case where the dielectric function depends only on the electron energy loss, for a homogeneous medium

$$1/\varepsilon_{\tau\tau'}(\omega) = [1/\varepsilon(\omega, \boldsymbol{\tau})]\delta(\boldsymbol{\tau}-\boldsymbol{\tau}')\delta(\tau_z - q_n). \quad (A.11)$$

Thus (*A*.10) becomes

$$I_v(\tau) = (e^2 k_0^2 V_s/\pi\varepsilon_0 v^2) \int_0^\infty \mathrm{d}\omega \int \mathrm{d}\mathbf{u}_b (u_b^2 + q_n^2)^{-1} \times \mathrm{Im}[-1/\varepsilon(\omega, \mathbf{u}_b)] |Z(\boldsymbol{\tau}-\mathbf{u}_b, \omega)|^2$$

$$= (e^2 k_0^2 V_s/\pi\varepsilon_0 v^2) \int_0^\infty \mathrm{d}\omega \{(\tau^2 + q_n^2)^{-1} \times \mathrm{Im}[-1/\varepsilon(\omega, \boldsymbol{\tau})]\} \otimes |Z(\boldsymbol{\tau}, \omega)|^2. \quad (A.12)$$

Therefore, the diffraction pattern is composed of the incoherent addition of all the electrons with different energy losses $\hbar\omega$ and momentum transfers, weighted by the probability functions. For the energy-filtered diffraction patterns of a narrow energy window, the integration of energy in (*A*.12) is dropped. It is important to note that (*A*.12) has the same form as (10) for localized inelastic scattering, thus the corresponding T function can be readily written as (23).

References

BIRD, D. M. & WRIGHT, A. G. (1989). *Acta Cryst.* **A45**, 104-109.
BORN, M. (1942). *Rep. Prog. Phys.* **9**, 294-333.
COWLEY, J. M. (1988). *Acta Cryst.* **A44**, 847-855.
COWLEY, J. M. & MOODIE, A. F. (1957). *Acta Cryst.* **10**, 609-619.
DOYLE, P. A. (1970). *Acta Cryst.* **A26**, 133-139.
EGERTON, R. F. (1986). *Electron Energy-Loss Spectroscopy in Electron Microscopes*. New York: Plenum Press.
FANIDIS, C., VAN DYCK, D., COENE, W. & VAN LANDUYT, J. (1989). In *Computer Simulation of Electron Microscope Diffraction and Images*, edited by W. KRAKOW & M. O'KEEFE, pp. 135-158. London: The Minerals, Metals and Materials Society.
GJØNNES, J. (1966). *Acta Cryst.* **20**, 240-249.
GJØNNES, J. & WATANABE, D. (1966). *Acta Cryst.* **21**, 297-302.
HALL, C. R. & HIRSCH, P. B. (1965). *Proc. R. Soc. London Ser. A*, **286**, 158-177.
HØIER, R. (1973). *Acta Cryst.* **A29**, 663-672.
HOWIE, A. (1963). *Proc. R. Soc. London*, **271**, 268-287.
ISHIZUKA, K. (1982). *Acta Cryst.* **A38**, 773-779.
ISHIZUKA, K. & UYEDA, N. (1977). *Acta Cryst.* **A33**, 740-749.
KOHL, K. & ROSE, H. (1985). *Adv. Electron. Electron Phys.* **65**, 173-227.
LOANE, R. F., XU, P. & SILCOX, J. (1991). *Acta Cryst.* **A47**, 267-278.
PALIK, E. D. (1985). Editor. *Handbook of Optical Constants of Solids*. New York: Academic Press.
REIMER, L., FROMM, I. & NAUNDORF, I. (1990). *Ultramicroscopy*, **32**, 80-91.
REZ, P., HUMPHREYS, C. J. & WHELAN, M. J. (1977). *Philos. Mag.* **35**, 81-96.
ROSSOUW, C. J. (1985). *Ultramicroscopy*, **16**, 241-254.
ROSSOUW, C. J. & BURSILL, L. A. (1985). *Acta Cryst.* **A41**, 320-328.
SELF, P. & O'KEEFE, M. (1989). In *High-Resolution Transmission Electron Microscopy and Associated Techniques*, edited by J. M. COWLEY, P. BUSECK & L. EYRING, pp. 244-307. New York: Oxford Univ. Press.
WANG, Z. L. (1990). *Phys. Rev. B*, **41**, 12818-12836.
WANG, Z. L. (1991). *Acta Cryst.* **A47**, 686-698.
WANG, Z. L. (1992). *Philos. Mag.* **B65**, 559-587.
WANG, Z. L. & BENTLEY, J. (1991*a*). *Ultramicroscopy*, **38**, 181-213.
WANG, Z. L. & BENTLEY, J. (1991*b*). *Microsc. Microstruct. Microanal.* **2**, 301-314.
WANG, Z. L. & BENTLEY, J. (1991*c*). *Inst. Phys. Conf. Proc.* No. 119, pp. 547-550.
WANG, Z. L. & BENTLEY, J. (1991*d*). *Microsc. Microstruct. Microanal.* In the press.
WANG, Z. L. & BENTLEY, J. (1991*e*). In *Proc. 49th Annu. Meet. Electron Microsc. Soc. Am. (San Jose)*, edited by G. W. BAILEY & E. L. HALL, pp. 708-709. San Francisco Press.
WHELAN, M. J. (1965*a*). *J. Appl. Phys.* **36**, 2099-2103.
WHELAN, M. J. (1965*b*). *J. Appl. Phys.* **36**, 2103-2110.
YOSHIOKA, H. (1957). *J. Phys. Soc. Jpn*, **12**, 618-628.

Acta Cryst. (1992). **A48**, 688-692

Resolution Investigations of X-ray Three-Crystal Diffractometers

BY L. BRÜGEMANN, R. BLOCH, W. PRESS AND M. TOLAN

Institut für Experimentalphysik, Universität Kiel, Leibnizstrasse 19, *D*-2300 *Kiel* 1, *Germany*

(*Received* 10 *August* 1991; *accepted* 6 *March* 1992)

Abstract

The object of this study is the resolution of a three-crystal diffractometer (TCD) using perfect crystals as monochromator and analyser. It relates to the resolution as a function of the scattering vector **Q**. This information is crucial for the interpretation of high-resolution X-ray diffraction data obtained very close to reciprocal-lattice points. In this light we present the experimentally determined resolution of TCDs

0108-7673/92/050688-05$06.00